PERGAMON

International Journal of Heat and Mass Transfer 44 (2001) 443–456

International Journal of HEAT and MASS TRANSFER

www.elsevier.com/locate/ijhmt

# Boiling heat transfer on machined porous surfaces with structural optimization

Y.Y. Jiang, W.C. Wang*, D. Wang, B.X. Wang

*Department of Thermal Engineering, Tsinghua University, Beijing 100084, People's Republic of China*

Received 9 September 1999; received in revised form 9 February 2000

**Abstract**

Boiling heat transfer on porous surfaces needs further research for augmentation. Analysis of the microfilm evaporation and two-phase flow inside the microstructure was used to develop new microscale heat transfer model for boiling heat transfer on porous surfaces. Simulation results were used to study in detail the effects of fluid parameter and microstructure dimensions on the heat transfer performance during the bubble formation period. For boiling on porous surfaces with such working fluids as R11, R22, R134a and water, optimum microstructure dimensions were determined for the given conditions. The calculated results fit previous experimental data well. An experimental rig was developed to measure the pool boiling heat transfer to test the predictions of the optimization. The experimental data verified the optimization results. 

*Keywords:* Porous surfaces; Microscale heat transfer; Heat transfer augmentation; Pool boiling

## 1. Introduction

Industrial demands for more efficient boilers and evaporators have spurred the development of methods to increase boiling heat transfer performance. In addition, advanced technologies, such as microelectronics and astronautics, require even better boiling heat transfer performance.

Different kinds of boiling heat transfer enhancement technologies have been developed, among which, sprayed porous layers or manufacture porous surfaces are effective and widely used. As described by Nakayama et al. [1], matrix of potential nucleation sites can be produced by machining, poor welding, sintering or brazing of particles, electrolytic deposition, flame spraying, bonding of particles by plating, galvanizing or plasma spraying of a polymer, or metallic coating of a foam substrate. Machined porous surfaces (Fig. 1) may have stable high performance, low cost and the microstructure dimensions can be accurately controlled. The artificial microstructure provides stable nucleation sites to trap vapor so that initial bubble formation can occur at wall superheats even lower than 1°C. Furthermore, these sites can promote heat transfer rates 3–10 times higher than that on a smooth surface.

As shown in Fig. 1, many rows of micropores may be distributed on the surface and linked to each other by microchannels under the surface. When heated in liquid pool, the channels nucleate first at very low wall superheat. Then, vapor produced in the channel flows, facing the liquid out through some active pores. Very thin film will adhere to the corners of the microchannels, forming liquid meniscuses. Liquid in these meniscuses con-

* Corresponding author.

0017-9310/01/$ - see front matter 
PII: S0017-9310(00)00057-0

**Nomenclature**

| | | | |
|---|---|---|---|
| $A$ | area ($m^2$) | $x$, $y$, $z$ | coordinates (Fig. 2) |
| $\bar{A}$ | Hamaker constant | $H$, $W$, $L_x$ | dimensions (Fig. 3) |
| $a_0$, $a_1$, $a_2$ | constants in Eq. (17) | $\alpha$ | accommodation coefficient |
| $d$ | diameter | | |
| $f$ | friction coefficient | $\delta$ | film thickness (m) |
| $G$ | mass flow rate (kg/s) | $\gamma$ | half angle of the corner |
| $g$ | gravity accelerate ($m/s^2$) | $\mu$ | dynamic viscosity (Pa s) |
| $h$ | coefficient of heat flux ($W/m^2$ K) or enthalpy (J/kg) | $\nu$ | kinematic viscosity ($m^2/s$) |
| $k$ | conduct coefficient (W/m K) | $\theta$ | meniscus contact angle |
| $m$ | mass (kg) | $\rho$ | density ($kg/m^3$) |
| $\dot{m}$ | evaporating mass flux ($kg/m^2$ s) | $\sigma$ | surface tension (N/m) |
| $M$ | molecular weight | $\tau$ | time (s) |
| $N$ | number of pores ($1/cm^2$) | $\Pi$ | disjoining pressure (Pa) |
| $N_A$ | number of active pores ($1/cm^2$) | *Subscripts* | |
| $N_L$ | number of injecting pores on one side of active pore ($1/cm^2$) | b | bubble |
| | | e | evaporate or equivalent |
| $p$ | pressure (Pa) | ex | outside |
| $q$ | heat flux ($W/m^2$) | l | liquid |
| $R$ | gas constant (kJ/kg K) | m | meniscus |
| | | o | pore |
| $T$ | temperature (K) | s | saturation |
| $u$ | internal energy (J/kg) | t | channel |
| | | v | vapor |
| $V$ | volume ($m^3$) | w | wall |
| $w$ | velocity in $z$ direction (m/s) | 0 | at $z = 0$ |
| | | 1 | at $z = N_L l_t$ |
| $l_t$, $d_0$, $d_e$, $s_{lid}$, $h_t$, $w_t$, $s_{wall}$ (mm) | dimensions (Fig. 1) | | |

tinually evaporates, making the bubbles on the active pores grow and depart over a very short period. When the bubbles are expanding, the pressure inside the channel goes down, which makes the liquid in the outer pool flow into the channel through inactive pores. This liquid flows to supply the liquid that has evaporated. This process is driven by capillary force produced by liquid–vapor surface tension. The intensive evaporation not only augments the evaporation heat transfer, but also augments the convective heat transfer. This is the so-called suction–evaporation mode. At still lower superheats, most of the channel space is occupied by liquid, and an active pore operates like an isolated nucleation site. This is the flooded mode. At larger superheats, the increased number of active sites and pressure inside the channels prevent liquid from entering through the pores into the channels. In this mode, called the dried mode, the porous surfaces operate like a smooth surface. Both the flooded mode and the dried mode are not desirable.

Boiling heat transfer on porous surfaces is affected by many factors such as the working fluid, the wall material, the shape and dimensions of the microstructure, the saturation conditions and so on. Various researchers have experimentally investigated the boiling and two-phase flow mechanisms to determine how the microstructure affects the heat transfer performance [2–4]. Nakayama et al. [2] and Cai and Deng [3] established the physical and mathematical models. However,

these models could not explain how the microstructure shape and size affect the heat transfer, and introduced so many experimental coefficients which strongly limit their applicability. In short, previous research has shown that:

1. The evaporating heat flux on porous surfaces is the predominant part of the total heat transfer and intensifies the convective heat transfer on porous surfaces [2].
2. Porous surfaces with better heat transfer performance do not necessarily have more active pores, or larger bubble formation frequency [3].

   These two conclusions imply that enhancing the heat transfer performance on porous surfaces requires improvement of the evaporation of thin film meniscuses inside the channels.
3. In the suction–evaporation mode [5], the radius of the meniscus inside the channels, $r_m$, is equivalent to the capillary radius, $r_c$. The gravitational effect can be neglected. The liquid and vapor velocities are very small. The vapor flow, thereby, will be incompressible and its boundary-layer can be approximated as one-dimensional, by which the liquid flow can be considered as quasi-one-dimensional [6].

These features are very similar to those for the heat transfer and two-phase flow inside the micro heat pipe (MHP) [5]. The model established in this paper is based on these assumptions.

## 2. Theoretical analysis and modeling

The sketch in Fig. 2 shows a typical channel section used for the model. One bubble formation period can be divided into two stages. The time from the previous bubble departure to the moment the new one appeared is the first stage. This is the pressure build-up stage, the vapor velocity is almost zero, which would be very short and can be simplified. The second stage begins when the bubble diameter, $d_b$, is equal to the pore diameter, $d_0$, and ends when the bubble departs. During this stage, vapor pressure inside the channel decreases, so this is the pressure reduction stage [2]. Only the bubble on the center active pore keeps growing, while the bubbles on the other pores are suppressed. Vapor produced in the channel flows through the active pore. Some pool liquid is sucked in through the inactive pores and flows along the channel corners driven by capillary force.

The right-half section in Fig. 2 is to be studied as below.

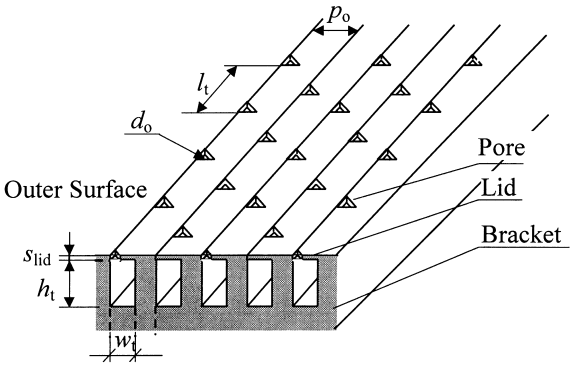


Fig. 1. Sketch of machined porous surfaces microstructure.

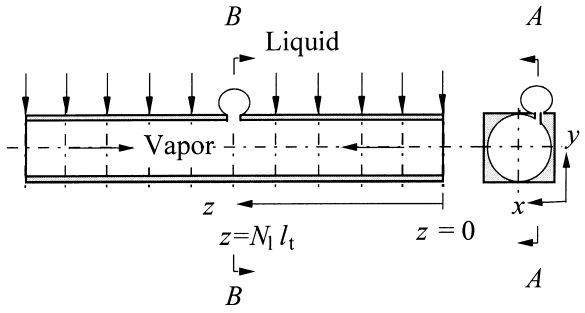


Fig. 2. Sketch map of liquid film distribution and two-phase flow inside tunnel.

### 2.1. Mass conservation equation

$$\bar{w}_l = \frac{\int_{A_l} w_l \, dx \, dy}{A_l} \tag{1}$$

$$\bar{w}_v = \frac{\int_{A_v} w_v dx \, dy}{A_v} \tag{2}$$

For meniscus shown in Fig. 3:

$$W = r_m \sin\left(\frac{\pi}{2} - \gamma - \theta\right) = r_m \cos(\gamma + \theta) \tag{3}$$

$$H = W/\tan\gamma, \qquad L_x = W/\sin\gamma \tag{4}$$

$$A_l = N r_m^2 \left[\frac{\cos(\gamma+\theta)}{\sin\gamma} \times \cos\theta - \left(\frac{\pi}{2} - \gamma - \theta\right)\right] \tag{5}$$

$$A_v = A_t - A_l \tag{6}$$

$$G_l = \rho_l \cdot \bar{w}_l \cdot A_l, \qquad G_v = \rho_v \cdot \bar{w}_v \cdot A_v \tag{7}$$

In differential form, the mass conservation equation is:

$$-\frac{\partial G_l}{\partial z}-\frac{\partial G_v}{\partial z}=\rho_l\frac{\partial A_l}{\partial \tau}+\rho_v\frac{\partial A_v}{\partial \tau}\approx\rho_l\frac{\partial A_l}{\partial \tau} \tag{8}$$

### 2.2. Momentum conservation equation for vapor

Because $u$, $v\approx 0$, the vapor flow is considered to be one-dimensional. In microstructure, the momentum conservation equation for vapor can be written as:

$$\rho_v\left(\frac{\partial w_v}{\partial \tau}+w_v\frac{\partial w_v}{\partial z}\right)=-\frac{dp_v}{dz}+\mu_v\left(\frac{\partial^2 w_v}{\partial x^2}+\frac{\partial^2 w_v}{\partial y^2}+\frac{\partial^2 w_v}{\partial z^2}\right) \tag{9}$$

Using $\bar{w}_v$ or $G_v$ and incompressible one-dimensional boundary-layer approximation [6], Eq. (9) can be written as:

$$\rho_v\left(\frac{\partial \bar{w}_v}{\partial \tau}+\beta_v\frac{\partial \bar{w}_v^2}{\partial z}\right)=-\frac{dp_v}{dz}-f_v\frac{2\rho_v\bar{w}_v^2}{D_{e,\,v}}, \tag{10}$$

$$\frac{\partial(G_v/A_v)}{\partial \tau}+\frac{\beta_v}{\rho_v}\frac{\partial(G_v/A_v)^2}{\partial z}=-\frac{dp_v}{dz}-f_v\frac{2G_v^2}{D_{e,\,v}\rho_v A_v}, \tag{11}$$

where.

$$\beta_v=1.33-0.0075Re_r^2,\qquad f_v=\left(16+0.25Re_r^2\right)/Re_r \tag{12}$$

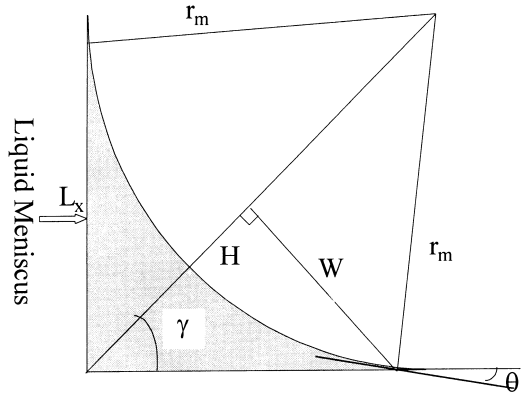


Fig. 3. Dimensions in a film meniscus.

### 2.3. Momentum conservation equation for liquid

For the liquid inside the channel:

$$\rho_l\left(\frac{\partial w_l}{\partial \tau}+w_l\frac{\partial w_l}{\partial z}\right)=-\frac{dp_l}{dz}+\mu_l\left(\frac{\partial^2 w_l}{\partial x^2}+\frac{\partial^2 w_l}{\partial y^2}+\frac{\partial^2 w_l}{\partial z^2}\right). \tag{13}$$

Using $\bar{w}_l$ and an incompressible quasi one-dimensional flow approximation, Eq. (13) can be written as:

$$\rho_l\left(\frac{\partial \bar{w}_l}{\partial \tau}+\bar{w}_l\frac{\partial \bar{w}_l}{\partial z}\right)=-\frac{dp_l}{dz}+\mu_l\left(\frac{\partial^2 \bar{w}_l}{\partial x^2}+\frac{\partial^2 \bar{w}_l}{\partial y^2}+\frac{\partial^2 \bar{w}_l}{\partial z^2}\right). \tag{14}$$

This equation was solved by Khrustalev and Faghri [4] with the Ritz method in terms of $r_m$ functions. They defined:

$$V(\gamma,\theta,F)=\iint_{A_l}\frac{w_l(x,y)\mu_l}{HW^3\left[\frac{dp_l}{dz}+\rho_l\left(\frac{\partial \bar{w}_l}{\partial \tau}+\bar{w}_l\frac{\partial \bar{w}_l}{\partial z}\right)\right]}dx\,dy, \tag{15}$$

where

$$F=-\frac{f_v\rho_v\bar{w}_v^2}{2W\left[\frac{dp_l}{dz}+\rho_l\left(\frac{\partial \bar{w}_l}{\partial \tau}+\bar{w}_l\frac{\partial \bar{w}_l}{\partial z}\right)\right]}. \tag{16}$$

For relatively small values of $\bar{w}_v$, the results can be approximated as:

$$V(\gamma,\theta,F)=\left(a_0+a_1\theta+a_2\theta^2\right)e^F, \tag{17}$$

where $\theta$ is in degrees. $a_0$, $a_1$ and $a_2$ are constants related to $\gamma$, whose values are given in the table in Ref. [8] for $F=0$. The relationship between $V$ here and $\bar{w}$ in Ref. [8] is:

$$V=\bar{W}\frac{L_x^2A_l}{HW^3} \tag{18}$$

For example, when $\gamma=30^\circ$ (triangle channel), $a_0=0.0241$, $a_1=9.05\times10^{-4}$, $a_2=8.75\times10^{-6}$. When $\gamma=45^\circ$ (square channel), $a_0=0.01253$, $a_1=1.506\times10^{-4}$, $a_2=6.5\times10^{-5}$. Therefore,

$$\frac{\partial(G_l/A_l)}{\partial \tau}+\frac{1}{2A_l\rho_l}\frac{\partial}{\partial z}\left(\frac{G_l^2}{A_l}\right)=-\frac{dp_l}{dz}+\frac{\mu_lG_l}{W^3HV\rho_l} \tag{19}$$

### 2.4. Energy conservation equation

The energy equation is established as:

$$(Q + G_l h_l + G_v h_v) - \left[G_l h_l + G_v h_v + d(G_l h_l) + d(G_v h_v)\right] = \frac{\partial(m_l u_l)}{\partial \tau} + \frac{\partial(m_v u_v)}{\partial \tau} \tag{20}$$

or:

$$q_p b_t - \frac{\partial(G_l h_l)}{\partial z} - \frac{\partial(G_v h_v)}{\partial z} = \frac{\partial\left(\rho_l A_l u_l\right)}{\partial \tau} + \frac{\partial\left(\rho_v A_v u_v\right)}{\partial \tau} \tag{21}$$

### 2.5. Additional equations

Eqs. (8), (11), (19) and (21) have five unknowns: $G_l$, $G_v$, $p_l$, $p_v(T_v)$, $r_m$. Additional equations are needed to close the model.

Augmented Young–Laplace equation [5]: At the liquid–vapor interface inside the channel,

$$p_l - p_v = -\frac{\sigma}{r_m} - \Pi, \tag{22}$$

where $\Pi = -\bar{A}/\delta_0^3$ is the disjoining pressure and $\bar{A}$ is Hamaker constant, which reflect the effects on the pressure difference due to intermolecular forces in the microliquid film. When $\delta_0 > 0.1$ μm, this term can be neglected.

Kelvin–Clapeyron equation: Wayner et al. [16] expanded the Kelvin–Clapeyron equation to account for the variation in the equilibrium vapor pressure with superheat and disjoining pressure in the thin film as:

$$\dot{m} = \frac{a(T_w - T_v) + b(p_l - p_v)}{1 + k_l h_{lv} a/\delta} \tag{23}$$

where

$$a = \left(\frac{2\alpha}{2-\alpha}\right)\left(\frac{M}{2\pi R}\right)^{\frac{1}{2}} \frac{V_l h_{lv}}{T_{lv} T_v R}, \qquad b = \left(\frac{2\alpha}{2-\alpha}\right)\left(\frac{M}{2\pi R}\right)^{\frac{1}{2}} \frac{V_l p_l}{T_{lv} R} \tag{24}$$

According to Eq. (23), evaporation is promoted by superheat and hindered by low liquid film pressure. For a thick film, the second term can be neglected and Eq. (23) becomes the conventional heat transfer equation.

In a liquid film meniscus A:

$$\overline{T_w - T_v} = \frac{\int_{A_x} \dot{m} h_{lv}\, dA_x}{\int_{A_x} (T_w - T_v)\, dA_x} \tag{25}$$

So,

$$q = \dot{m} h_{lv} = \bar{h}_e \cdot \overline{(T_w - T_v)} \tag{26}$$

CFD analysis showed that the heat flux was mostly in the radial direction. The film thickness can be written as a function of $x$ (Fig. 2):

$$\delta = \left[(x - b_t/2 + L_x)^2 + r_m^2 - 2r_m(x - b_t/2 + L_x)\cos(\pi/2 + \theta)\right]^{\frac{1}{2}} - r_m \tag{27}$$

Therefore, the solution of the governing equations, Eqs. (8), (11), (19), (21)–(23), describes the heat transfer and two-phase flow inside the channel. The basic assumptions are:

1. The vapor flow is considered to be incompressible and one-dimensional. The liquid flow is viscous and quasi-one-dimensional.
2. Gravitational force can be neglected.
3. The dissipation heat produced by friction is not included.
4. The radiative heat transfer is negligible.
5. Pure material.
6. The evaporation takes place only along the liquid meniscus.

The six unknowns are $G_l$, $G_v$, $p_l$, $p_v(T_v)$, $r_m$ and $T_w$. Once the wall superheat $T_w - T_v$ is determined, the averaged heat transfer coefficient $\bar{h}_e$ can be calculated by Eq. (26).

### 2.6. Simplified pressure build-up stage

The pressure build-up stage begins at the end of the pressure-reduction stage. For the microchannel system in consideration, the time $\Delta\tau$ can be determined as:

$$qF_t\Delta\tau = (m_l u_l + m_v u_v)|_{\tau=0} - (m_l u_l + m_v u_v)|_{\tau=\tau_{end}} \tag{28}$$

### 2.7. Initial and boundary conditions

For a round pore, the friction coefficient, including the inlet effect for the liquid flowing through the pore is [15]:

$$f'_v = 0.115\frac{d_0}{s_{lid}} + \frac{17.31}{Re} \tag{29}$$

The values for pores of other shapes are given by Rohsenow et al. [13]. Note that Eq. (29) is for large channels and that the friction characteristics of microchannels differ from those of conventional channels. However, there is no reliable method for calculating the friction coefficients of the microchannels. Experimental results suggest that $f'_v$ should be increased to $f_v = 1.76f'_v$, therefore,

$$G_{l,\,ex}(i) = (p_s - p_l)\frac{\pi d_0^3}{8 f_v s_{lid}\rho_l} \quad i = 1, 2, \ldots, N_l \tag{30}$$

The suction liquid mass flux, $G(i)_{l,\,ex}$ of inactive pore, $i$, can then be calculated from Eq. (30).

The boundary conditions at $z = 0$ are: $G_v|_{z=0} = 0$, $G_l|_{z=0} = G(0)_{l,\,ex}/2$.

Cai and Deng [3] used the following equation to calculate the vapor pressure at $z = l_t N_L$:

$$p_{v,1} - p_s = 4\sigma/d_b - H_s\rho_l + \Delta p_{vf} + \Delta p_{li}, \tag{31}$$

where $\Delta p_{vf}$ is the friction loss for vapor flow through the active pore and $\Delta p_{li}$ is the inertia force term of the liquid phase surrounding the growing bubble. $H_s\rho_l \approx 0$. $d_b$ can be calculated from:

$$V_b = \int_0^\tau 2\left(G_{v,l}/\rho_v\right) d\tau \tag{32}$$

$$d_b = \left(\frac{8}{c_l}\right)^{\frac{1}{3}} \cdot 2\left(\frac{3V_b}{4\pi}\right)^{\frac{1}{3}}, \tag{33}$$

where, $c_l = (1 + \cos\theta)[\sin^2\theta + (1 + \cos\theta)^2]$

$\Delta p_{vf}$ can be calculated from:

$$\Delta p_{vf} = 4 f_v \frac{s_{lid}}{d_0} \cdot \frac{1}{2}\rho_v \bar{u}_v \tag{34}$$

According to Ayyaswamy et al. [7],

$$\Delta p_{li} = 0.0011847 c_l^{2/3}\rho_l d_b \left[\frac{1}{\rho_v V_b^{2/3}}\frac{\partial G_v}{\partial \tau} - \frac{4}{3V_b^{5/3}}\left(\frac{G_v}{\rho_v}\right)^2\right]. \tag{35}$$

At $\tau = 0$, Nakayama et al. [2] show that:

$$G_v = 0, \quad G_l = 0, \quad G_{ex,\,i} = 0, \quad p_v(z)|_{\tau=0} = p_s + 4\sigma/d_0,$$

$$p_l(z)|_{\tau=0} = p_s.$$

### 2.8. Determination of $N_L$ and $N_A$

The distribution of number of active pores, $N_A$, on porous surfaces are irregular. However, the artificial nucleation sites may be regular, so the active pores should be distributed on the surface equably and the number of inactive pores, $N_L$, for either side of every active pore should be uniform.

Suppose the number of inactive pores on one side of a active pore is $N_L$. During the pressure-reduction stage, vapor flow along the channel towards the center active pore produces a pressure drop. Therefore, inactive pores that are farther from the center have higher vapor pressures $p_A$, with less liquid injected through the pores. If for a given inactive pore, during the whole stage:

$$p_v - (p_s + 4\sigma/d_0) \geq 0 \tag{36}$$

Then, this pore cannot receive any liquid. Since this would violate the suction–evaporation mode condition, this pore must be the one farthest away. Khrustalev and Faghri [4] provided a simplified equation to calculate the pressure drop along the evaporating microchannel,

$$p_{v,\,0} - p_{v,\,1} = c_f\rho_v\left(4|Re_r| + \frac{4}{3}Re_r^2\right)\left(\frac{4z\upsilon_v}{d_{e,\,v}^2}\right)^2 \tag{37}$$

We use it with $c_f = 16.4$ and $Re_r \approx \frac{q}{h_{lv}\rho_v}\frac{d_{e,\,v}}{\upsilon_v}$ to determine $z_{max}$. Then, the number of pores, $N = N_A + 2N_L - 1$.

## 3. Simulation results and discussion

### 3.1. Computational flow

The equations were solved numerically in finite difference form by iteration with over-relaxation in

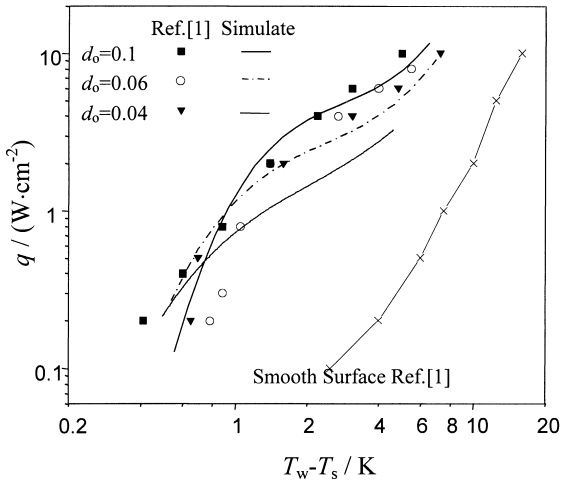


Fig. 4. Boiling curves in R11.

recessive Euler method. The calculation flow is as following:

1. Compute $V_{dp}$, and $N_L$ and determine initial values of all variables.
2. Derive $V_b$ and $p_{v,1}$ using Eq. (31) at $\tau = \tau + \Delta\tau$.
3. Calculate $p_v(z)$, $p_l(z)$ and $r_m(z)$ in the reverse $z$ direction.
4. Calculate $G_{l,ex}(i)$, $G_v(z)$, $G_l(z)$ and $T_w(z)$ in the forward $z$ direction. Then, use these new values to compute $p_v(z)$ iteratively again.

   Repeat Steps 3 and 4 with over-relaxation form until the new values of $p_v(z)$ converge.
5. Solve the average wall superheat and heat transfer coefficient. Repeat Steps 2, 3 and 4 until $V_b > V_{dp}$.

### 3.2. Model verification

The results were compared with the experiment data of Nakayama et al. [1,2]. As shown in Fig. 4, for the three surfaces, the values and trends predicted by the model fit well with the experimental data. At low heat fluxes, the predictions for the surface with pores of $d_0 = 0.06$ mm are somewhat higher than experimental data. At high heat fluxes, the predictions for the surface with pores of $d_0 = 0.04$ mm are somewhat smaller than experimental data. Some of these differences may be due to experimental uncertainty. The experimental data for the surface with $d_0 = 0.06$ mm pores deviate much from those for the other surfaces, and the experimental data for the surface with $d_0 = 0.06$ mm pores are also much larger than those in Ref. [3].

The calculated results for the number of active pores are compared with the experimental data in Nakayama et al. [1,2] in Fig. 5. At moderate heat fluxes, the calculated results fit the experimental data well. When heat fluxes becomes so large that $N_L = 129.85$ 1/cm$^2$, and $N_A/N = 1/2$, i.e., there is only one inactive pore between two nearby active pores. If heat fluxes increases further, the system will change to the dried mode.

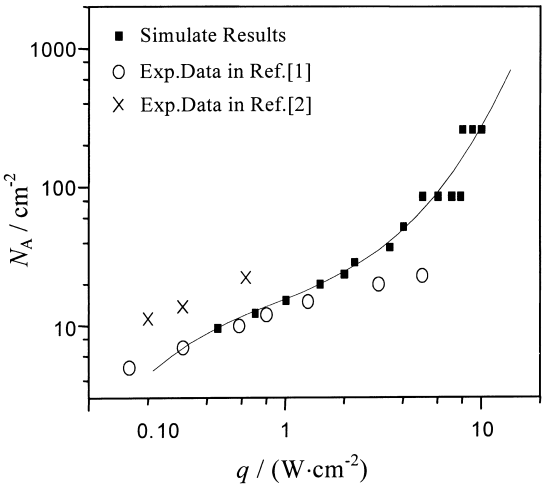


Fig. 5. Number of active pores.

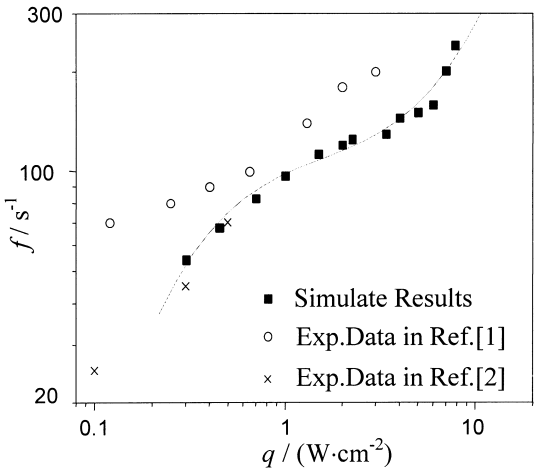


Fig. 6. Averaged bubble formation frequency.

The results for the bubble departure diameter, $d_{dp}$, and the bubble formation frequency, $f$, determined from different equations differ greatly. Following Ref. [4],

$$d_{dp} = \left[\frac{6d_0\sigma}{(\rho_l - \rho_v)g}\right]^{1/3} \tag{38}$$

We have the calculated values of the frequency less than the experimental data in Ref. [1] but agree well with data given by Ref. [2], as shown in Fig. 6.

### 3.3. Investigation of some parameters

The proposed analytical model was used to perform a systemic survey for the heat transfer and two-phase flow mechanism inside the channels and the variation of some parameters during the bubble formation period for the porous surfaces with microstructure dimensions listed in Table 1. The temporal variations of several important parameters at $z = 0.56$ mm are given in Fig. 7.

Table 1
Microstructure dimensions being investigated

| $d_0$ (mm) | $d_e$ (mm) | $h_t/w_t$ | $l_t$ (mm) | $s_{lid}/d_0$ |
|---|---|---|---|---|
| 0.1 | 0.3 | 1 | 0.7 | 2 |

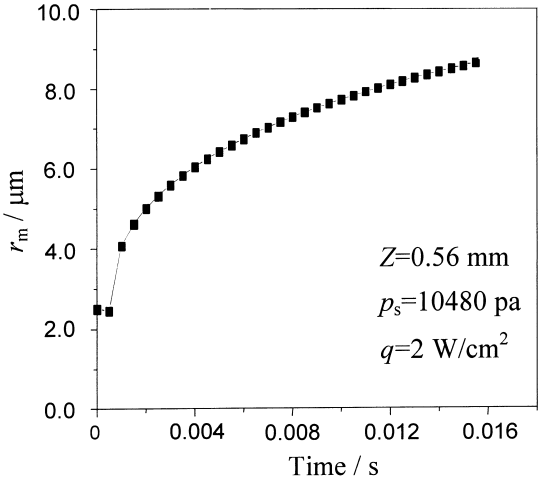


Fig. 7. Liquid meniscus radius variation (R11).

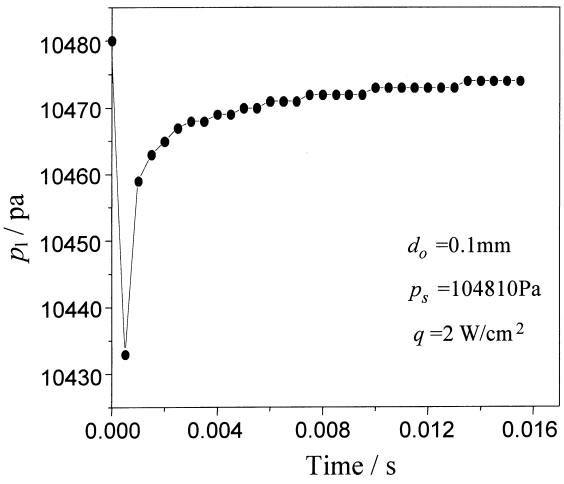


Fig. 9. Meniscus liquid pressure (R11).

During the pressure build-up stage, some liquid flows into the channel through inactive pores, which causes the liquid meniscus radius, $r_m$, to increase (Fig. 7). The data in Fig. 8 verified the basic assumption that the vapor pressure decreases during the pressure-reduction stage.

As shown in Fig. 9, the meniscus liquid pressure, $p_l$, as a function of the vapor pressure, $p_v$, and the meniscus radius, $r_m$, may either increase or decrease. The initial conditions assume that the vapor is not moving, that is, $p_{v,1} - p_s = 4\sigma/d_b$. However, at $\tau = \tau_0 + \Delta\tau$, the vapor suddenly has a velocity, then $p_{v,1} - p_s = 4\sigma/d_b + \Delta p_{vf} + \Delta p_{li}$, and a jump occurs in Figs. 8 and 9. Of course, the vapor velocity would not be exactly zero. Actually, the injected liquid may flood the channel, when boiling takes place on porous surfaces with $d_0 >$ 0.2 mm pores in water. In this case, $p_v$ will increase very rapidly in the direction opposite to the flow. When $p_l$ becomes larger than $p_s$, the liquid inside the channel will be ejected.

For liquid films with conventional dimensions, increasing the film thickness increase the heat transfer resistance. However, for microliquid film, Eq. (23) shows that evaporation in the micromeniscus increase with wall superheat and is hindered by low liquid film pressure. Neither thick nor thin microfilm is favorable for heat transfer. Comparing the values of $r_m$ in Fig. 7 with the values of $h$ in Fig. 10 shows this result. Therefore, there is an optimal microfilm thickness for a given heat flux. The heat transfer performance of porous surfaces can be enhanced by optimizing the microstructure so that the liquid meniscus thickness inside the channel maximizes the evaporation.

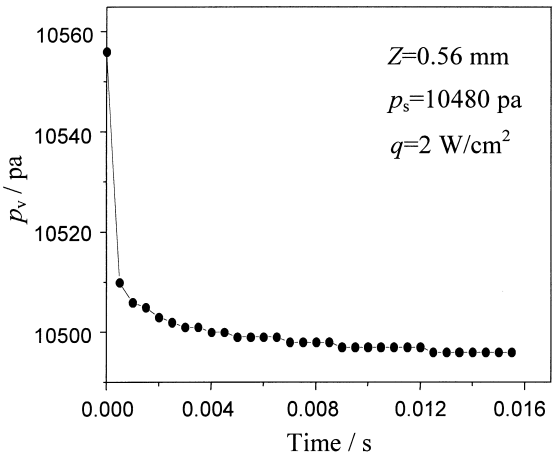


Fig. 8. Vapor pressure inside channel (R11).

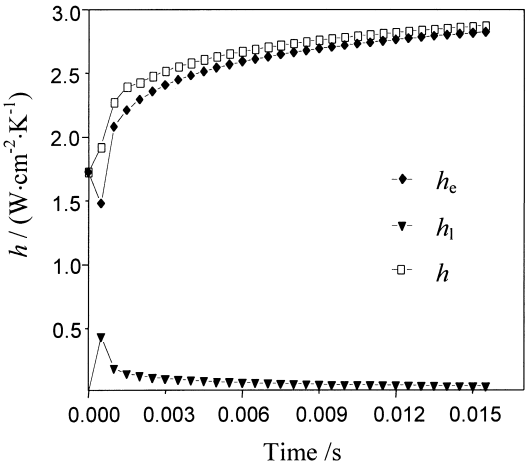


Fig. 10. Heat transfer coefficient.

Table 2
Optimized porous surfaces of microstructure

| | $d_0$ (mm) | $d_e$ (mm) | $h_t/b_t$ | $l_t$ (mm) | $s_{lid}/d_0$ |
|---|---|---|---|---|---|
| R11 | 0.09 | 0.35 | 1 | 0.6 | 2.5 |
| Water | 0.15 | 0.40 | 3 | 0.50 | 1 |
| R22 | 0.07 | 0.30 | 1 | 0.60 | 1.5 |
| R134a | 0.08 | 0.40 | 1 | 0.55 | 1 |

As shown in Fig. 10, the convective heat flux due to the liquid flow is only a small part of the total heat flux, that is $h_l/h < 10\%$. However, Deng et al. [3] found that the ratio is $h_l/h = 30$–$40\%$, further experiments are needed to clarify this.

### 3.4. Optimization of the microstructure

The model was used to optimize the porous surfaces structure for boiling in R11, R22, R134a and water. For industrial conditions, the surface tension of R11 is twice that of R22 while their other properties are similar. Water is polar fluid with much larger surface tension and heat of vaporization. The different optimized dimensions, Table 2, shows the effects of these properties.

#### 3.4.1. Pore diameter $d_0$

Among all the dimensions, $d_0$ affects the heat transfer performance the most. It determines the friction of liquid or vapor flowing through the micropore. The results derived here are consistent with the data in Nakayama et al. [1] and Deng et al. [3] (for R11, $d_{0,\,opt} = 0.1$ mm, for water, $d_{0,\,opt} = 0.14$ mm), as shown in Fig. 11. The optimized $d_0$ of working fluids with large surface tensions and heats of vaporization are also large. Eq. (22) shows that the vapor pressure inside the channel of the fluid with larger surface tension is also larger, which is not favorable for liquid suction. Therefore, larger pore, which reduces the flow friction, is preferable.

#### 3.4.2. Channel hydraulic diameter $d_e$

The equivalent channel diameter, $d_e$, determines the channel's two-phase flow performance and the liquid film distribution. Like $d_0$, the optimized $d_e$ of working fluids with large surface tensions and heats of vaporization are also large (Fig. 12). For fluids with larger surface tensions, Eqs. (22) and (23) show that the liquid–vapor pressure difference at the interface affects the heat resistance more and thicker liquid film is better for evaporation. Larger $d_e$ is favorable for reducing vapor pressure inside the channel that causes more liquid to flow in during the pressure-reduction stage. For some conditions, more than one optimum $d_e$ was found for water. This interesting phenomena cannot be explained by this model.

#### 3.4.3. Channel height to width ratio, $h_t/w_t$

Channels with different channel height to width ratio, $h_t/w_t$, would have different flow resistance, and hence, the ratio affects the heat transfer performances as shown in Fig. 13. For organic fluids, the best ratio is around 1–2, while, for water, 2–4 is better.

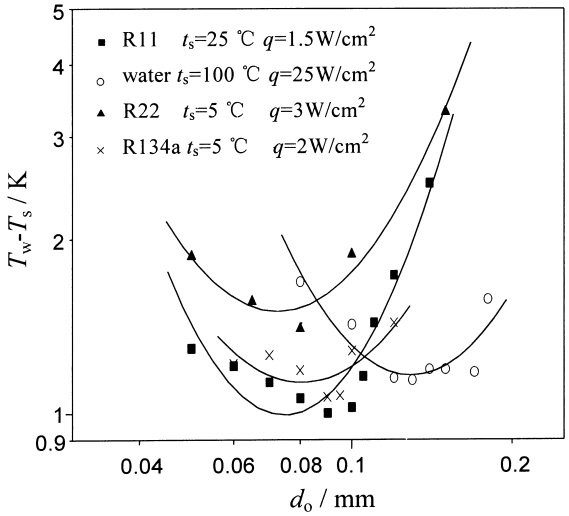


Fig. 11. Heat transfer performance of porous surfaces with different $d_0$.

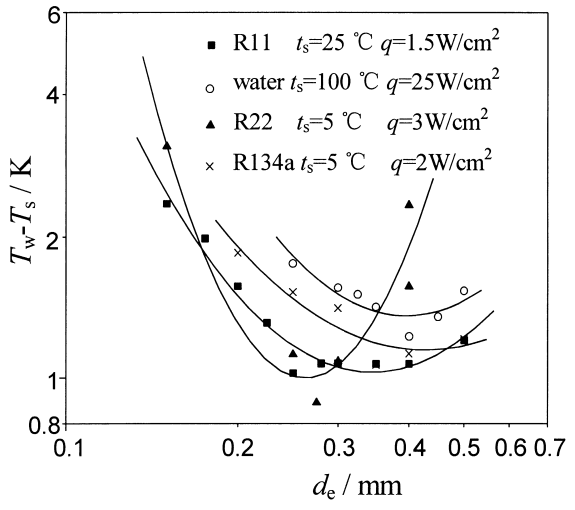


Fig. 12. Boiling heat transfer performance of porous surfaces with different $d_e$.

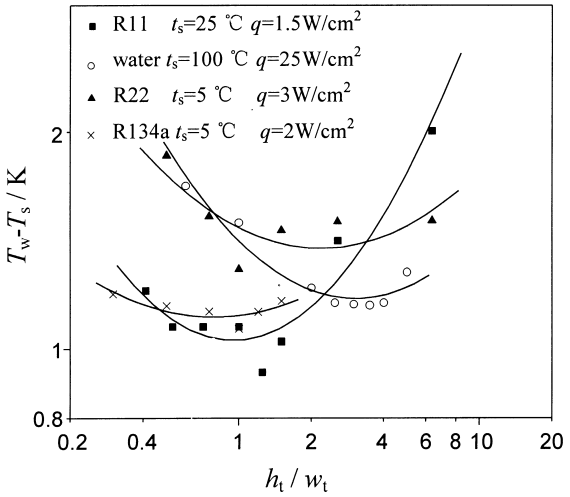


Fig. 13. Heat transfer performance of porous surfaces with different $h_t/w_t$.

*3.4.4. Space between two pores $l_t$*

The space between two pores determines how many inactive pores can absorb liquid per active pore. The optimized distance is strongly affected by the heat flux. For liquids with low surface tension, thinner films favor evaporation, and larger $l_t$ would be preferable (Fig. 14).

*3.4.5. Channel lid thickness to pore diameter, $s_{lid}/d_0$*

During the pressure-reduction stage, the vapor pressure varies rapidly if the liquid has larger surface tension. For this kind of media, a larger ratio would be better (Fig. 15).

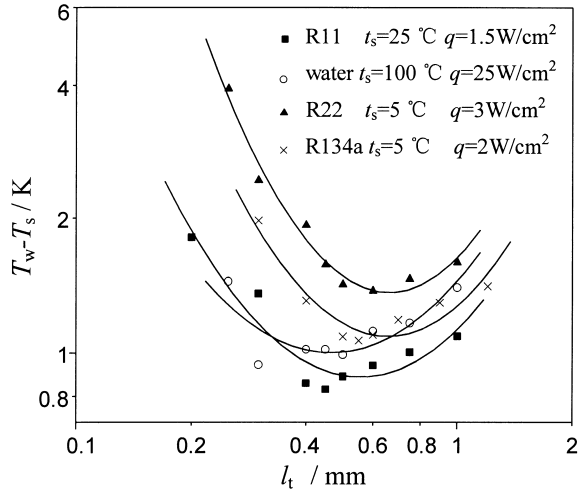


Fig. 14. Boiling heat transfer performance of porous surfaces with different $l_t$.

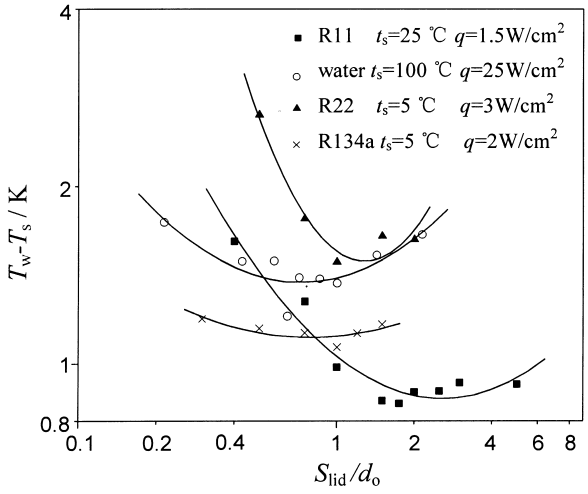


Fig. 15. Boiling heat transfer performance of porous surfaces with different $s_{lid}/d_0$

*3.4.6. Channel shape*

This model can be conveniently applied to analyze the boiling heat transfer of porous surfaces with other polygon cross sections. Fig. 16 shows that the hexagonal channels with the same $d_e$ (listed in Table 3) is the best one for moderate heat fluxes among the three shapes. However, at high heat fluxes, the hexagonal channel tends to dry out, and the heat transfer rate deteriorates very rapidly.

## 4. Experiments

Of the microstructure parameters optimized using the model, only the results of the pore diameter $d_0$

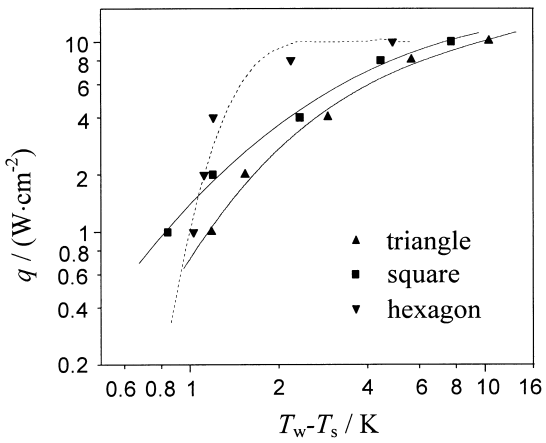


Fig. 16. Boiling heat transfer rate of porous surfaces with different channel's cross sections.

Table 3
The microstructures with different channel's shapes

| $d_0$ (mm) | $d_e$ (mm) | $l_t$ (mm) | $p_t$ (mm) | $s_{lid}$ (mm) |
|---|---|---|---|---|
| 0.1 | 0.3 | 0.55 | 0.55 | 0.2 |

were verified by experimental data in open literature. However, the results discussed show that the microchannel hydraulic diameter, $d_e$, and the channel height to width ratio, $h_t/w_t$ can also strongly affect the boiling heat transfer performance of the porous surfaces. A pool boiling heat transfer experimental rig was built to check the effects of $d_e$ and $h_t/w_t$.

### 4.1. Experiment setup

The experiment system (Figs. 17 and 18) consists of a experiment setup, a data acquisition unit, a DC regulator, an AC manostat, a precise manometer and a water cooling system.

A working liquid pool is contained in the space formed by a glass tube and two covers. Boiling occurs on a porous surfaces heater heated by a heating unit with constant power supplied by the DC regulator. The heater wall surface and pool temperatures are measured by type-T thermocouples, and recorded by the data acquisition unit. Saturation occurs only if the vapor pressure measured by the manometer is equal to the saturation pressure at the measured pool temperature. The AC manostat is connected to the assistant heater in the pool. A manual valve is mounted in the water cooling loop. The assistant heater and the loop are used to regulate the saturation temperature of the pool.

The whole heating unit is well insulated. As shown in Fig. 18, a rectangular steel block (0.5% carbon), whose conductivity, $k_{Fe}$ is known, lies between the heating plate and the porous surfaces heater. A $3 \times 4$ (row distance $\Delta z = 10$ mm) of thermocouples is attached to the block. The temperature differences when the heat flows through the block is used to calculate the heat flux, i.e.

$$q_{i,j} = \frac{T_{i,1+j} - T_{i,1}}{j\Delta z} k_{Fe} \quad i = 1, 2, 3, 4, j = 1, 2 \tag{39}$$

The heat unit is considered as stable only if this heat flux value is equal to that measured from the heater. The steel block is attached to the porous surfaces heater by silicon rubber glue and the temperature difference of the joint is less than 5°C.

The porous surfaces heating unit (Fig. 19), is manufactured by welding (solder melting point = 200°C) a copper block with five parallel rectangular microgrooves and a copper tinsel (0.05 mm) with five rows of pores. The microgrooves are machined by electrical incision and their width and height are changed systemically as listed in Table 4. The precision for the

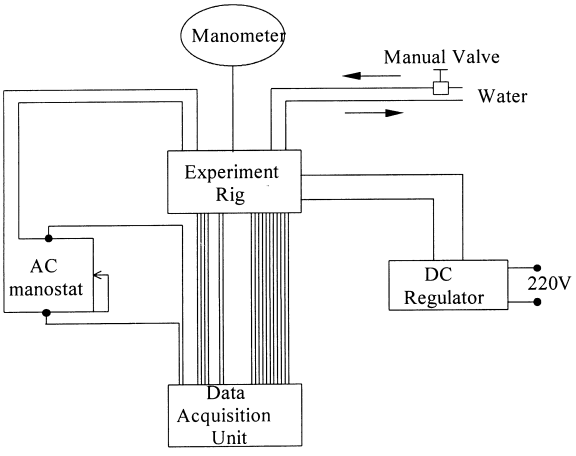


Fig. 17. System layout.

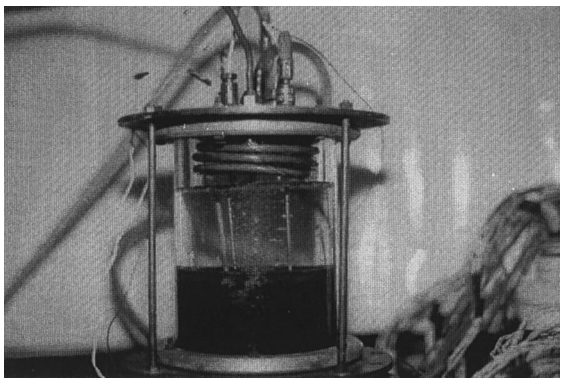

Fig. 18. Photograph of the experiment rig.

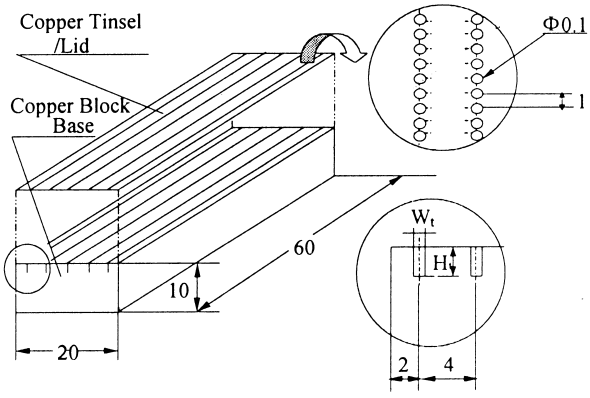


Fig. 19. Diagram of porous surfaces heating unit.

dimensions and spacing are within ±1 μm. The pores on the plate, with a diameter 0.1 mm, are made by a highly precise laser boring device with precision of ±2 μm and ±1 μm for spacing precision. The row pitch of the plate and the block are the same. The solder is very thin, so the thermal contact resistance between the plate and the block is negligible. Four thermocouples to measure the heating wall surface temperature are not embedded in the upper surface but on the section 5 mm below the surface, so that the boiling liquid field is not disturbed. The wall temperature, $T_w$, can be calculated from the section temperatures, the heat flux and the copper block's thermal conductivity.

The four copper blocks in each column of Table 4 have the same hydraulic diameters, $d_e$, but different ratios, $h_t/w_t$. The four in each row have the same $h_t/w_t$ with different $d_e$. So, comparison of the heat transfer rates of those porous surfaces will illustrate the effects of $h_t/w_t$ or $d_e$.

Technical limitations requested the use of a microchannel pitch (4 mm) that is much larger than the optimum (0.5–1.00 mm), which results in lower heat transfer coefficients in the tested units than in normal commercial products. However, the relative values from the experiment are still useful.

The testing unit is cleaned by acetone and soaked in acetone for 24 h to remove the dirt and oil. The container is also cleaned. After installation, the experiment rig is exposed to a vacuum for 40 min, followed by filling with the working fluid, R11. Tests are carried out half a day later.

When heating began, the presence of non-condensable gases is detected if the indicated vapor pressure is larger than the saturation pressure related to the pool temperature. Such non-condensable gases are then discharged.

The unit is heated with the heat flux decreasing in step to avoid the effects of boiling hysteresis. The heating power is first increased to the highest (2 W/cm$^2$) and then decreased to the lowest (0.2 W/cm$^2$). Steady state is required for about halt an hour (that the heat flux value calculated from the heating power equals to that measured by the thermocouple matrix on the steel block). The boiling conditions are also recorded.

Table 4
Dimensions and shapes of the channels

| | $d_e$ (mm) | | | |
|---|---|---|---|---|
| $h_t/w_t$ | 0.29 | 0.35 | 0.50 | 0.60 |
| 6.35 | 0.17 × 1.06 | 0.20 × 1.27 | 0.29 × 1.84 | 0.35 × 2.20 |
| 2.57 | 0.20 × 0.51 | 0.24 × 0.62 | 0.35 × 0.89 | 0.42 × 1.07 |
| 1.5 | 0.24 × 0.36 | 0.29 × 0.43 | 0.42 × 0.62 | 0.50 × 0.75 |
| 1.0 | 0.29 × 0.29 | 0.35 × 0.35 | 0.50 × 0.50 | 0.60 × 0.60 |

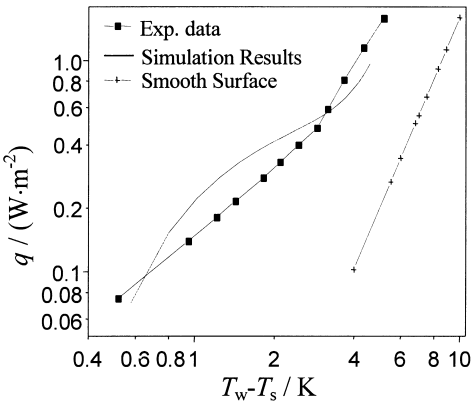


Fig. 20. Typical data for $d_e = 0.35$ mm, $h_t/w_t = 1$.

### 4.2. Experiment results and discussion

The smooth surface boiling heat transfer coefficient data for this experiment are very close to that of Nakayama et al. [1] (Fig. 20), The differences between the simulation results and the experimental data for the porous surfaces unit with $d_e = 0.35$ mm and $h_t/w_t = 1$ are also shown in Fig. 20 for illustration.

#### 4.2.1. Effects of channel hydraulic diameter, $d_e$

The experimental results suggest that the heat transfer performances of all the porous surfaces with $d_e = 0.35$ mm are better than the others with same $h_t/w_t$ but different $d_e$. The differences are greater for $h_t/w_t = 1$ (Fig. 21). The data supports that the optimum $d_e$ will be 0.35 mm. The simulation results imply that for moderate heat fluxes, the best diameter is 0.33 mm,

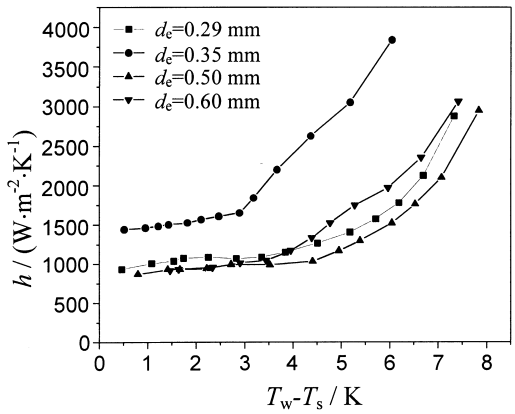


Fig. 21. Boiling heat transfer coefficients of porous surfaces with $h_t/w_t = 1$ and different $d_e$.

which is very close to the experiment result. For larger $h_t/w_t$, the heat transfer from the unit with channels of $d_e = 0.29$ mm seems to be the worst because the channels are too narrow, resulting in a much larger flow resistance for the vapor and the liquid. The experiments also showed that the heat transfer coefficient for the units with $d_e$ of 0.60 mm is usually higher than that of the unit with $d_e$ of 0.50 mm, which is not reflected in the calculation results. Consequently, the larger film surfaces of the channels with $d_e$ of 0.60 mm allows more liquid to evaporate, resulting in a higher heat transfer coefficient.

*4.2.2. Effects of channel height to channel width ratio, $h_t/w_t$*

As demonstrated in simulation results, the experiments suggest that the heat transfer from each porous surface with $h_t/w_t = 1$ should be better than the others with the same $d_e$ but different $h_t/w_t$ (Fig. 22), which supposes that the best rectangular channel is square. However, the effects of the aspect ratio are not as obvious as those of the diameter, especially when $d_e$ becomes fairly large. As the effects of the aspect ratio on the heat transfer are limited by the channel dimensions, no useful results could be obtained by merely optimizing the shape of the channels without optimizing the diameters. The results showed that the optimum $h_t/w_t$ ratio increases as $d_e$ increases. The best $h_t/w_t$ ratio for the porous surfaces with $d_e$ of 0.6 mm was 2.57. The average liquid film radius, $r_m$, of this porous surface with $d_e = 0.6$ mm is larger than 0.20 mm at a wall superheat of $T_w - T_s = 4°C$. So, all the microchannels are covered with very thick liquid films. The longer sides of the channels with high aspect ratios cause the film to be thinner, which results in a smaller heat resistance and consequently, makes the evaporation heat transfer greater.

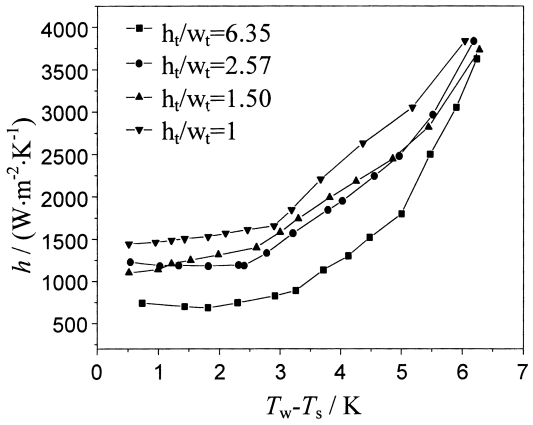


Fig. 22. Boiling heat transfer coefficients for porous surfaces with $d_e = 0.35$ mm and different $h_t/w_t$.

## 5. Conclusions

1. The heat transfer performance of porous surfaces is augmented by enhancing the evaporation of the thin liquid films inside the microchannels. All the dimensions of the microstructure markedly affect the heat transfer performance. Therefore, the evaporation can be enhanced by selecting the best shape and dimensions of the microstructure so that the liquid film has the smallest thermal resistance.
2. The surface tension and evaporation of the working fluids are the two most important properties. For boiling on porous surfaces in fluids with large surface tensions, it is suitable to choose larger pore diameter, $d_0$, thick lid, larger channel hydraulic diameter, $d_e$, and smaller space between two pores, $l_t$. Some of these conclusions were proved by previous and present experiments and others will be verified by further experiment investigations.
3. A pool boiling heat transfer experimental rig was built to research the effects on heat transfer of the channel hydraulic diameter, $d_e$, and the channel height and width ratio, $h_t/w_t$ of the porous surfaces. The experiment results show that the channel optimum $d_e$ depends on the $h_t/w_t$ ratio and vice versa. However, the effect of the $h_t/w_t$ ratio is limited by the diameter, $d_e$. The comprehensive optimum $h_t/w_t$ ratio and $d_e$ are consistent with the simulation results.
4. To enlarge the heat transfer area inside the channels, and to prevent the film from becoming too thick, the porous surfaces should have sharp channel corner angles, rough surfaces and crossed channels.
5. There is more than one optimum $d_e$ for water for some conditions. This interesting phenomenon needs to be studied further.
6. The convective heat flux due to liquid convection in the channels is only a small part of the total heat flux, which does not agree with the conclusion drawn by Deng et al. [3]. Experiments are needed to clarify this.
7. The calculated pressure jump at the beginning of the pressure-reduction stage implies that at $\tau = 0$, the vapor velocity is not actually zero. This velocity should be measured experimentally.

## Acknowledgements

The project is supported by the National Natural Science Foundation of China (Grant number: 59995550-3).

## References

[1] W. Nakayama, T. Daikoku, H. Kuwahara, T. Nakajima, Dynamic model of enhanced boiling heat transfer on porous surfaces. Part 1: Experimental investigation and Part 2: Analytical modeling, ASME Journal of Heat Transfer 102 (3) (1980) 445–456.

[2] W. Nakayama, T. Daikoku, T. Nakajima, Effects of pore diameters and system pressure on saturated pool nucleate boiling heat transfer from porous surfaces, ASME Journal of Heat Transfer 104 (1) (1982) 286–291.

[3] B. Cai, S. Deng, Investigation of boiling heat transfer mechanism and performance of mechanically fabricated porous surfaces, Proceedings of Joint Meeting of Chemical Engineering of CIESC and AICHE 2 (1982) 664–671.

[4] D. Khrustalev, A. Faghri, Thermal analysis of a micro heat pipe, J. Heat Transfer 116 (1994) 189–198.

[5] G.F. Hewitt, C.L. Tien, Micro Scale Energy Transport, Taylor & Francis, USA, 1998.

[6] N. Akio, K. Matsutaro, Effect of bubble frequency on bubble departure diameter in nucleate pool boiling, Heat Transfer Japanese Research 16 (1984) 32–47.

[7] P.S. Ayyaswamy, I. Catton, D.K. Edwards, Capillary flow in triangular grooves, ASME Journal of Heat Transfer 96 (1) (1974) 332–336.

[8] A.E. Bergles, Heat transfer enhancement — the maturing of second-generation heat transfer technology, Heat Transfer Engineering 18 (1) (1997) 47–55.

[13] W.M. Rohsenow, J.P. Hartnett, N.G. Ejup, Handbook of Heat Transfer Fundamentals, McGraw-Hill, New York, 1985.

[15] S. Yilmaz, J.W. Palen, J. Taborek, Enhanced boiling surfaces as single tubes and tube bundles, Advances in Eng. Heat Transfer, ASME HTD 31 (1982) 123–129.

[16] P.C. Wagner, Jr., Y.K. Kao, L.V. La Croix, The interline heat transfer coefficient of an evaporating wetting film, Int. J. Heat Mass Transfer 19 (1976) 487–491.